arXiv:1204.1151v1 [astro-ph.SR] 5 Apr 2012

Numerical simulations of chromospheric hard X-ray source sizes in solar flares

M. Battaglia [1,2], E. P. Kontar [1], L. Fletcher [1]

and

A. L. MacKinnon[1]

SUPA, School of Physics and Astronomy, University of Glasgow, G12 8QQ, UK

Institute of 4D Technologies, School of Engineering, University of Applied Sciences and Arts Northwestern Switzerland, 5210 Windisch, Switzerland

`e-mail: marina.battaglia@fhnw.ch`

ABSTRACT

X-ray observations are a powerful diagnostic tool for transport, acceleration, and heating of electrons in solar flares. Height and size measurements of X-ray footpoints sources can be used to determine the chromospheric density and constrain the parameters of magnetic field convergence and electron pitch-angle evolution. We investigate the influence of the chromospheric density, magnetic mirroring and collisional pitch-angle scattering on the size of X-ray sources. The time-independent Fokker-Planck equation for electron transport is solved numerically and analytically to find the electron distribution as a function of height above the photosphere. From this distribution, the expected X-ray flux as a function of height, its peak height and full width at half maximum are calculated and compared with RHESSI observations. A purely instrumental explanation for the observed source size was ruled out by using simulated RHESSI images. We find that magnetic mirroring and collisional pitch-angle scattering tend to change the electron flux such that electrons are stopped higher in the atmosphere compared with the simple case with collisional energy loss only. However, the resulting X-ray flux is dominated by the density structure in the chromosphere and only marginal increases in source width are found. Very high loop densities ($> 10^{11}\mathrm{cm}^{-3}$) could explain the observed sizes at higher energies, but are unrealistic and would result in no footpoint emission below about 40 keV, contrary to observations. We conclude that within a monolithic density model the vertical sizes are given mostly by the density scale-height and are predicted smaller than the RHESSI results show.

Subject headings: Sun: flares – Sun: X-rays, γ-rays – Sun: Chromosphere

1. Introduction

The transport of flare-accelerated electrons and the generation of hard X-ray (HXR) emission in the solar atmosphere is one of the most important and widely used diagnostics of flare accelerated electrons. These supra-thermal particles precipitate along the field lines of a magnetic loop from the acceleration site towards the denser regions of the chromosphere. They undergo Coulomb collisions with electrons and ions in the ambient plasma, and can be observed via their bremsstrahlung emission. The bulk of the observed HXR emission comes from the footpoints of magnetic structures where the density is high and electrons lose their energy completely, with the electron stopping location (depth) determined by the initial electron energy and the ambient density.

Using this energy dependency in combination with observations from RHESSI (Lin et al. 2002), it has become possible to characterize the structure of X-ray sources. Assuming collisional transport, the chromospheric density could be inferred (Aschwanden et al. 2002; Kontar et al. 2008, 2010; Saint-Hilaire et al. 2010; Battaglia & Kontar 2011). These observations suggest that the bulk of HXRs in the range 30-100 keV is produced at heights of $\sim 0.7 - 1.2$ Mm. The density scale heights generally agree well with hydrostatic chromospheric density models such as (e.g. Vernazza et al. 1981). However, using RHESSI visibility techniques (Hurford et al. 2002; Schmahl et al. 2007), it is also possible to infer the energy-dependent source sizes with better than arcsecond accuracy as shown by Battaglia & Kontar (2011); Kontar et al. (2008, 2010). The source sizes in the direction along the magnetic field inferred by these authors are in the range from 2 arcsec to 6 arcsec (Battaglia & Kontar 2011) which is up to a factor of 4 larger than what would be expected from collisional transport in the same density profile. To explain this discrepancy, Kontar et al. (2010) suggested that the electrons propagate in a multi-thread loop with different density profiles along each thread, so that the X-ray source positions are the same as in the case of collisional transport in a single density loop, but the vertical size is enlarged. However, even within a single monolithic loop, Battaglia & Kontar (2011) indicated a number of processes which might increase the vertical extent of HXR sources.

To investigate those effects quantitatively one has to solve the equations for electron transport in the footpoints. The electron transport problem has been considered in the past by several authors to investigate various aspects of electron transport, electron trapping and energy losses in the solar atmosphere. Both semi-analytical and full numerical solutions can be found in the literature. Leach & Petrosian (1981); Kovalev & Korolev (1981); Bai (1982); McClements (1990, 1992), and Kocharov et al. (2000) use numerical methods to investigate the effect of the magnetic field geometry and magnetic trapping on the electron spectrum while MacKinnon & Craig (1991) use a test-particle method of solution, applying it to a situation without magnetic mirroring. Many of those studies focused on the electron transport and the effect of scattering and magnetic mirroring on the electron distribution. To compare these models with actual observations, one has to go a step further and model the resulting X-ray flux, as was done by e.g. Leach & Petrosian (1983). With the observational capabilities of instruments such as Yohkoh and RHESSI it became possible to directly compare the models with observations. Petrosian & Donaghy (1999) investigate the conditions for formation of loop-top sources and compare predicted time-profiles of the X-ray emission with time-profiles observed by Yohkoh. Minoshima et al. (2008) use a trap-plus-precipitation model to explain RHESSI observations. While those studies all focused on spectra, Fletcher (1996) investigated the height of X-ray sources obtained from numerical simulations and compared them with Yohkoh observations, finding that they are consistent with partial electron trapping in a magnetic trap. However, there are no quantitative studies of the HXR source sizes.

In this paper, we focus on the size of HXR sources produced by non-thermal electrons ($E \gtrsim 30$ keV) in Coulomb collisions with the ambient plasma. Within the assumption of a single monolithic loop we analyze a range of processes which could increase the vertical extent (along the magnetic field lines) of the sources and explain the observations. Thus we consider: i) density variations in a single loop; ii) the role of the initial pitch angle distribution iii) the effect of pitch-angle scattering; iv) magnetic mirroring, and v) instrumental effects related to RHESSI observations.

2. Transport of energetic electrons in X-ray footpoints

The evolution of an initial electron flux distribution $F_0(E_0, z)$ as a function of distance z along the magnetic field lines is described by the time independent Fokker-Planck equation (e.g. Holman et al. 2011, as a recent review), including magnetic mirroring and collisional pitch-angle scattering and energy loss:

$$\frac{\partial F}{\partial z} - \frac{1-\mu^2}{2\mu}\frac{\mathrm{d}(\ln B)}{\mathrm{dz}}\frac{\partial F}{\partial \mu} - \frac{Kn(z)}{\mu E}\frac{\partial F}{\partial E} + \frac{n(z)K}{2E^2\mu}\frac{\partial}{\partial \mu}\left[(1-\mu^2)\frac{\partial F}{\partial \mu}\right] = -\frac{Kn(z)}{\mu E^2}F, \qquad (1)$$

where $n(z)$ is the plasma density at distance z, $K = 2\pi e^4 \Lambda$, with Λ the Coulomb logarithm, B is the magnetic field strength, and μ is the cosine of the electron pitch angle relative to the magnetic field direction. In the case of purely collisional energy loss in a uniform magnetic field and an injected electron power-law flux distribution $F_0(E_0) \sim E_0^{-\delta}$ this leads to:

$$F(E, z) = F_0[E_0(E, z)]E\sqrt{E^2 + 2KN(z)}^{(-\delta-1)}, \qquad (2)$$

where $E_0(E,z) = (E^2 + 2KN(z))^{1/2}$ and $N(z) = \int n(z)dz$ is the column depth. This we will refer to as "simple thick-target" in this paper. Equation 1 can also be solved analytically by neglecting collisions but including the term for the magnetic field (e.g. Leach & Petrosian 1981; Zweibel & Haber 1983). However, this analytical solution is only applicable as long as the electron pitch angle cosine is larger than about 0.7 because of a factor $\sim 1/\mu$ that is introduced in Eq. 2. Thus, if one wants to include all physical effects one has to use test-particle simulations. Equation 1 can be written as a set of stochastic differential equations (e.g. Kovalev & Korolev 1981; Fletcher 1996). Since the typical integration time necessary for reliable imaging of footpoints with RHESSI is of the order of 30 - 60 seconds, which is very large compared to the electron loop transit time and collisional loss time in the chromosphere, a time-independent treatment is a good approximation. Therefore we consider time-independent equations along the particle path:

$$
\begin{aligned}
\frac{dz}{ds} &= \mu && (3)\\
\frac{dE}{ds} &= -\frac{K}{E}n(z) && (4)\\
\frac{d\mu}{ds} &= -(1-\mu^2)\frac{d\ln B}{2dz} - \frac{\mu K n(z)}{E^2} + \left[(1-\mu^2)\frac{Kn(z)}{E^2}\right]^{1/2} W, && (5)
\end{aligned}
$$

where z is the distance from the point of injection along the magnetic field lines, s is the path of the electron, and $W(s)$ denotes a standard Wiener process. Equations 3-5 are solved using a numerical scheme:

$$
\begin{aligned}
z_{j+1} &= z_j + \mu_j \Delta s && (6)\\
E_{j+1} &= \left[E_j^2 - 2Kn(z_j)\Delta s\right]^{1/2} && (7)\\
\mu_{j+1} &= \mu_j - \frac{1}{2}(1-\mu_j^2)\frac{d\ln B}{dz}\bigg|_{z=z_j} \Delta s - \frac{\mu_j K n(z_j)}{E_j^2}\Delta s + \left[(1-\mu_j^2)\frac{Kn(z_j)}{E_j^2}\Delta s\right]^{1/2} \xi, && (8)
\end{aligned}
$$

where ξ is a random variable taken from the normal distribution $p(\xi) = 1/\sqrt{2\pi}\exp(-\xi^2/2)$ for each step Δs. The scheme proved to be reliable in modelling the effect of collisional scattering on pitch angle (see Bai 1982; MacKinnon & Craig 1991). Equations (7-8) are solved using a power-law electron distribution

$$
F_0(E_0, h = h_{loop}) \sim E_0^{-\delta} \tag{9}
$$

injected at the top of the loop with high energy cutoff energy at 500 keV and injection height $h_{loop} = 12.5$ Mm. Equation 2 was used to test the simulations. Both numerical and analytical solutions result in the number of electrons as a function of distance z from the injection point, or, equivalently, as a function of height h above the photosphere $F(E,h)$

where $h = h_{loop} - z$. Finally, calculating the corresponding X-ray bremsstrahlung intensity $I(\epsilon, h)$, and determining the X-ray source vertical profiles, this is compared to observations made with RHESSI.

2.1. Definition of size and position

In the observations of limb events presented in Kontar et al. (2008, 2010) and Battaglia & Kontar (2011), we found the position and size by forward fitting X-ray visibilities (2D spatial Fourier components) with a circular or elliptical Gaussian source model. The size of a source is thereby defined as the full-width at half maximum (FWHM) of the fitted Gaussian.

$$I(x, y; \epsilon) = \frac{I_0(\epsilon)}{2\pi\sigma_x\sigma_y} \exp\left(-\frac{(x - x_0(\epsilon))^2}{2\sigma_x^2} - \frac{(y - y_0(\epsilon))^2}{2\sigma_y^2}\right), \tag{10}$$

where $2\sqrt{2\ln 2}\sigma_x$ and $2\sqrt{2\ln 2}\sigma_y$ are FWHMs of an elliptical Gaussian source in the x and y direction respectively. For HXR sources observed at the solar limb, the size along the radial direction represents the vertical FWHM size of the source, while the perpendicular size (along the solar limb) is equivalent to the size of a HXR footpoint parallel to the solar surface. The simulations performed here provide the electron flux as a function of height $F(E, h)$ (one dimension) and hence the vertical extent of HXR sources. The X-ray flux $I(\epsilon, h)$ per unit distance is then given as:

$$I(\epsilon, h) = \frac{n(h)A(h)}{4\pi R^2} \int_{\epsilon}^{\infty} F(E, h)\sigma(\epsilon, E)\mathrm{dE} \tag{11}$$

where $A(h)$ is the area of the magnetic flux tube at height h, R is the distance Sun-Earth and $\sigma(\epsilon, E)$ the bremsstrahlung cross-section.

We define the height of a source as the first moment of the X-ray flux profile and the FWHM as the second moment. Only emission larger than 10% of the maximum flux was used to compute the moments, to emulate the fact that RHESSI images have a limited dynamic range (Hurford et al. 2002). Figure 1 illustrates the photon flux as a function of height for two photon energies in the analytical solution of the simple thick-target case. The right-hand side of the figure shows the observed FWHM in the event analyzed in Kontar et al. (2010) compared with the expected FWHM in a simple thick-target model given by the analytical solution of Eqs. (2,11) .

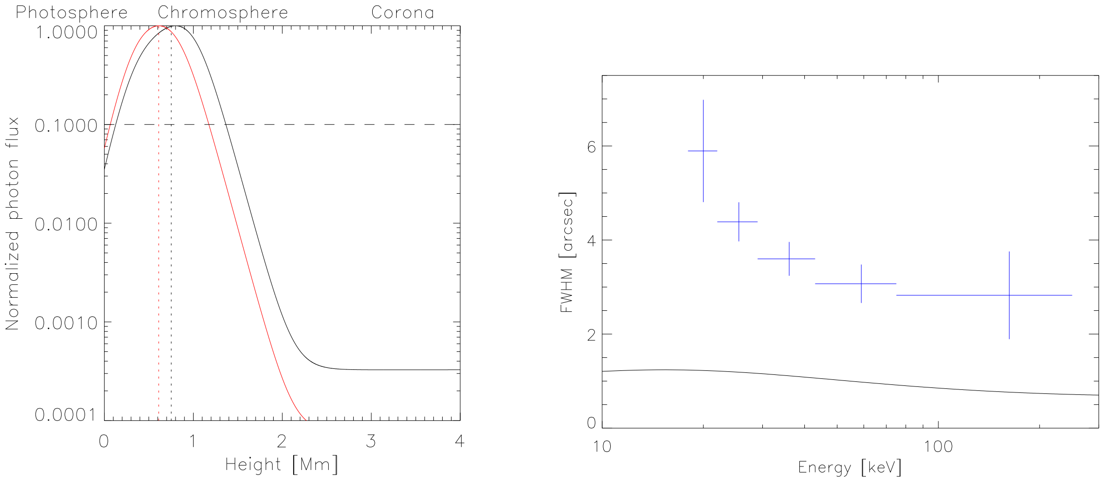

Fig. 1.— Left: Normalized photon flux as a function of height above the photosphere at 30 keV and 70 keV (red), using a density profile of $n(h) = 10^{10} + 1.16 \times 10^{17} \times exp(-h/h_0)$ (comp. Eq. 12) with a scale-height h_0=130 km. The vertical dashed lines give the first moment (maximum position) of the emission above 10 % (horizontal dashed line). Right: Observed FWHM in the event of January 6th 2004 (after Kontar et al. 2010). The black line is the expected source FWHM in a simple thick target, using Eqs. 2 and 11.

3. Analytical and numerical results

We first investigate the effect of the chromospheric density function on the resulting source size in the simple thick target (analytically), using Eq. 2. Then, the influence of the initial pitch-angle distribution, collisional pitch-angle scattering and magnetic mirroring will be explored using test-particle simulations (Eq. 3 - 5). Finally, in Section 3.7 we will discuss in more detail how the sources would be observed by RHESSI and what results we would expect using visibility forward fitting.

3.1. Chromospheric density structure

The deposition of large amounts of energy into the chromosphere by energetic electrons could lead to a number of processes, including heating and expansion of the chromosphere. This process of chromospheric evaporation generally leads to redistribution of plasma density in the flaring atmosphere, increasing the density of plasma in the flaring loop (Hirayama 1974; Antiochos & Sturrock 1978). At the same time, the density structure in a flaring loop can strongly affect the source size even in the case of purely collisional energy loss. In previous work, a single scale-height exponential density (Kontar et al. 2008, 2010; Battaglia & Kontar 2011), multiple scale-height density (Saint-Hilaire et al. 2010) or a power-law density function (Aschwanden et al. 2002) have been investigated. Although the positions of HXR sources are in agreement with the single scale-height exponential density profiles with scale heights of 130-200 km, the predicted vertical source sizes are up to a factor of 4 smaller than observed (Battaglia & Kontar 2011) (Kontar et al. (2010) suggested that a multi-threaded density structure with vertical strands of different density could increase the source size significantly). The exponential density function

$$n(h)^{exp} = n_l + n_{phot} \times exp(-h/h_0) \tag{12}$$

is used by Battaglia & Kontar (2011) where n_l is the (constant) loop density, $n_{phot} = 1.16 \times 10^{17}$ cm^{-3} the photospheric density following Vernazza et al. (1981), and h_0 is the density scale height. Figure 2 illustrates such an exponential density model with scale-height h_0=130 km, and also a density model of the shape of a κ-function

$$n(h)^{\kappa} = n_{phot} \times \left(1 + \frac{h}{\kappa h_0}\right)^{(-\kappa+1)}, \tag{13}$$

for a κ factor of 10 and two different scale heights $h_0 = 130$ km and $h_0 = 290$ km (dark blue and light blue curves in Fig. 2). In addition, densities that combine the exponential function near the photosphere with either a quadratic function or a κ-function at larger heights were used, where the exponential plus quadratic function was given as $n(h) = n(h)^{exp} + 1.16 \times 10^{a}(h_{max} - h)^2$, where h_{max} is the loop height and $a = [10, 11, 12]$ (yellow, dark red, and red curves in Fig. 2). The exponential plus κ-function was given as $n(h) = n(h)^{exp} + n(h)^{\kappa}$ (green curve in Fig. 2). These latter models account for the fact that the high density in the lower chromosphere, below about 1 Mm, will not be affected significantly by processes such as evaporation (Machado et al. 1980), while the loop density may be considerably different from quiet Sun density models. As Fig. 2 demonstrates, a notable effect on the FWHM is only found if the loop density reaches extreme values of more than 10^{11} cm^{-3}. Such coronal densities are rather non-typically high although are observed in some flares (e.g. Veronig et al. 2006). Such high densities will lead to energetic electrons of energy $\sim$ 20 keV and even higher being collisionally stopped in the coronal part of the loop before reaching the chromospheric footpoints.

All these density functions result in an effective increase of the loop density compared with the single scale-height exponential and the resulting HXR source FWHM is larger by up to a factor of 4 than in the case of an exponential density (Fig. 2). However, the location of the peak of the emission is also found to be a factor of 4 higher, and the bulk of the emission below 40 keV comes from the top of the coronal loop, therefore no footpoints would be observed below 40 keV, which is not the case in the observations (Battaglia & Kontar 2011), where footpoints are observed at energies as low as 20 keV.

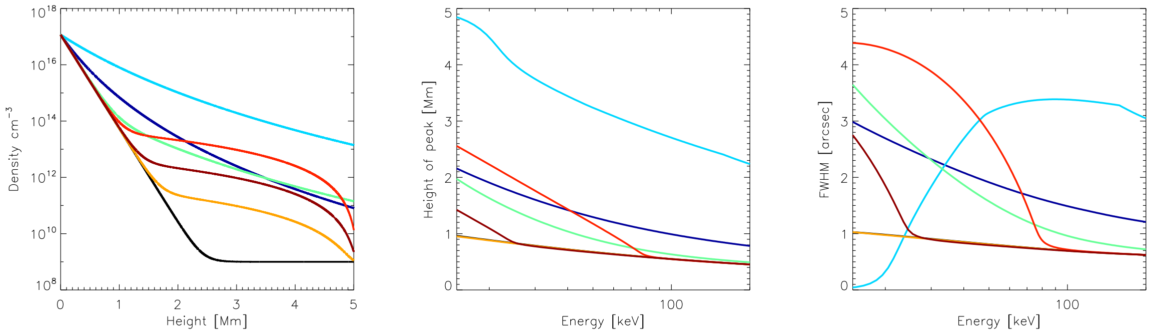

Fig. 2.— Effect of different density models on the height and FWHM of HXR sources. Left: Density models. The black curve is an exponential density with a single scale-height of 130 km. Dark blue and light blue are κ-functions with different scale heights. Green is an exponential density combined with a κ-function. Yellow, red and dark red represent an exponential density combined with a $\sim h^2$ function (see text for details). Middle: Height of peak emission as a function of energy. Right: FWHM as a function of energy.

Due to the relatively modest increase of the chromospheric temperature at heights below 1 Mm, we assumed a neutral atmosphere. However, the plasma in the transition region and lower corona will be partially or completely ionized with a change in the ionization fraction at some height in the chromosphere. The ionization state of the medium affects the Coulomb logarithm, so that $\ln \Lambda_{eH} \simeq 7.1$ in neutral media and $\ln \Lambda_{ee} \simeq 20$ in fully ionized plasma, where Λ_{ee} and Λ_{eH} are the electron-electron and electron-hydrogen Coulomb logarithms. The effect of this on HXR spectra has been discussed by Brown (1973) and in the context of RHESSI spectroscopy by Kontar et al. (2002). To investigate the influence of ionization change on the height and the FWHM of HXR sources, we introduced an effective Coulomb logarithm

$$\Lambda = (\Lambda_{ee} - \Lambda_{eH}) \left(x(h) + \frac{\Lambda_{eH}}{\Lambda_{ee} - \Lambda_{eH}} \right), \tag{14}$$

The ionization fraction $x(h)$ was assumed to be a step function with $x(h) = 1$ for $h > 0.9$ Mm and $x(h) = 0$ for $h < 0.9$ Mm. The effect of non-uniform density is illustrated in Fig. 3 along with a comparison with the case of constant Coulomb logarithms. The case of a more realistic atmosphere with partial ionization would lead to results within the extremes illustrated in Fig. 3 and will not change the source size noticeably. Thus, the use of an idealized ionization structure is justified.

The simulations show that although different chromospheric and loop density models can increase the source size by up to a factor of 4 to fit the observations, this will also change the height of the sources, contrary to the observations. It has to be noted that in order to produce a noticeable change of the HXR source size, the density structure of the whole atmosphere, including the transition region and corona needs to be changed by a few

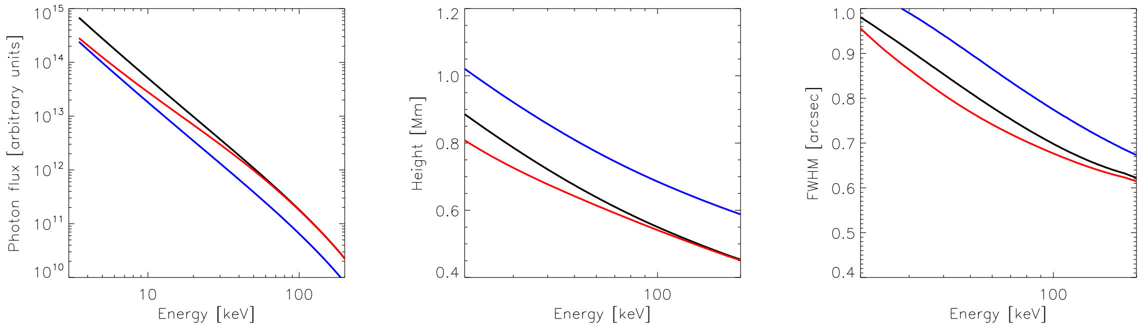

Fig. 3.— Left: Total photon spectra for completely neutral target (black), completely ionized target (blue) and ionization step-change (red). Middle and right: Height and FWHM of HXR sources as a function of energy in the three cases.

orders of magnitude. This seems in contradiction with both theoretical models of the flaring atmosphere (e.g. Allred et al. 2005) and observations.

3.2. Pitch-angle distribution

The height and the width of a source is also likely to depend on the initial pitch-angle distribution of the injected electron beam. In the simple thick-target model, injection and propagation of energetic electrons is assumed parallel to the magnetic field (i.e. cosine of initial pitch angle $\mu_0 = 1$), but in the other extreme case of injection perpendicular to the field ($\mu_0 = 0$) or strong trapping, the electrons would lose energy near the acceleration region, the height would be constant as a function of energy, and the FWHM would depend on the extent of the acceleration region. In an intermediate situation $0 < \mu_0 < 1$, energetic electrons are expected to lose energy at different heights depending on their initial pitch-angle distribution. The effect of an initial pitch-angle distribution is investigated including collisional energy loss, but no change in the initial pitch-angle distribution is assumed, i.e. Eq. 5 is $d\mu/ds = 0$. In this and the subsequent sections, an exponential density profile $n(h) = n_l + n_{phot} \exp(-h/h_0)$ with a scale height of 144 km and a constant Coulomb logarithm of $\Lambda = 7.1$ is used. This density profile is consistent with the source heights measured with RHESSI and the theoretical modeling of the low atmosphere at heights $h \lesssim 1$ Mm.

Figure 4 illustrates how the initial pitch-angle distribution affects the height and the FWHM. Three different cases are presented: $\mu_0 = 1$ (as a reference), $0.9 < \mu_0 \leq 1$ uniform (strongly beamed) and $0.1 < \mu_0 \leq 1$ uniform (broad distribution). The broad distribution leads, as expected, to a larger source size as a function of energy, as well as a larger FWHM. However, the maximum change in both height and FWHM is about 10% in the case of the broad distribution. Therefore, this effect alone cannot account lead to the observed vertical sizes of HXR sources.

3.3. Collisional pitch-angle scattering

In collisional interactions with the ambient plasma, electrons do not only lose energy, but are pitch-angle scattered with a similar rate. Therefore, their pitch-angle distribution changes as the particles propagate downwards towards dense regions of the atmosphere. Figure 5 compares the standard case (collisional energy loss only), with the outcome of a situation with collisional pitch-angle scattering included, i.e. Eq. 5 becomes

$$\frac{d\mu}{ds} = -\frac{\mu K n(z)}{E^2} + \left[(1-\mu^2)\frac{K n(z)}{E^2}\right]^{1/2} W. \tag{15}$$

In this case, the maximum emission is located up to 20 % higher than in the no-scattering case. However, the effect on the FWHM is small, at the level of about 5%. As expected, the effect is qualitatively similar to the injection of a broad initial pitch-angle distribution.

3.4. Magnetic mirroring

A converging magnetic field at the loop footpoints also changes the pitch-angle distribution of energetic electrons, causing electrons with large pitch angle (small $\cos\theta$) to mirror upwards from the footpoints before they are collisionally stopped. This might further contribute to an increase in source size. In this Section we consider collisional energy loss, and pitch-angle change due to magnetic field convergence, but not collisional pitch-angle change, i.e. Eq. 5 becomes $d\mu/ds = -(1-\mu^2)\frac{d\ln B}{2dz}$. The magnetic field strength is modeled as $B(h) = B_0 + B_1 \tanh(-(h-h_M)/h_M)$, which adequately represents a converging magnetic field in the chromosphere (Fedun et al. 2011). This model gives a magnetic field $B(h >> h_M) \rightarrow B_0 - B_1$ at coronal heights and $B(h=0) \rightarrow B_0 + B_1 \tanh(1)$ at the photospheric level. The increase in field strength relative to the ambient density is illustrated in Fig. 6. The field convergence (and the electron pitch angle) defines the depth of the mirroring point. If the magnetic field converged higher up in the loop, the sources would

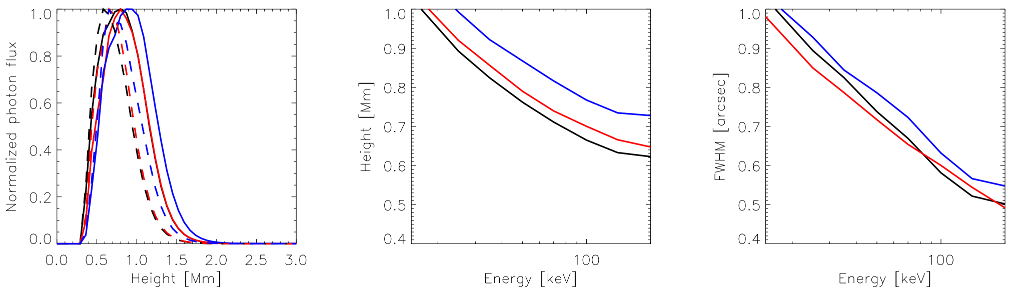

Fig. 4.— Normalized photon flux as a function of height at 30 keV and 70 keV (solid and dashed lines, left), height of maximum emission and FWHM as a function of photon energy (middle and left), for three cases of initial pitch-angle distribution: μ_0=1 (black), $0.9 < \mu_0 \leq 1$ (red), $0.1 < \mu_0 \leq 1$ (blue).

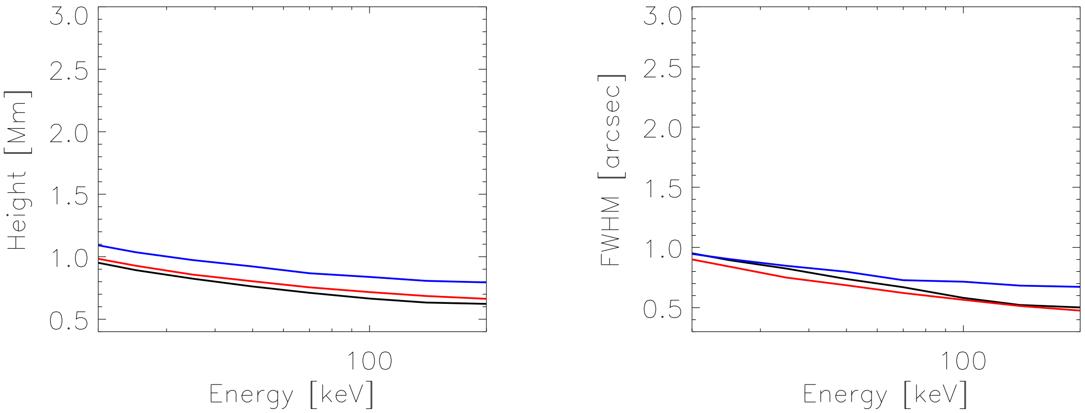

Fig. 5.— Height of maximum emission and FWHM as a function of photon energy (middle and left), for two cases of initial pitch-angle distribution: $0.9 < \mu_0 \leq 1$ (red), $0.1 < \mu_0 \leq 1$ (blue), and including collisional pitch-angle scattering. The black line indicates the result for collisional energy loss only.

be observed higher up. In the extreme case, one could simulate a coronal source caused by electron trapping.

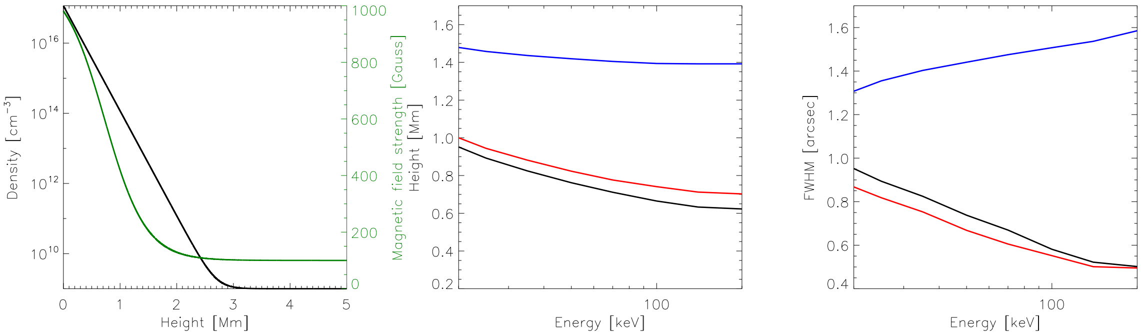

Fig. 6.— Left: Density and magnetic field strength as a function of height. Height of maximum emission and FWHM as a function of photon energy (middle and right), for two cases of initial pitch-angle distribution: $0.9 < \mu_0 \leq 1$ (red), $0.1 < \mu_0 \leq 1$ (blue), and including magnetic mirroring. The black line indicates the result for collisional energy loss only. $B(h) = B_0 + B_1 \tanh(-(h - h_M)/h_M)$ with $h_M = 1$ Mm, $B_0 = 600$ Gauss, $B_1 = 500$ Gauss.

In the case presented in Fig. 6, the source height is increased by a factor of ~ 1.6, while the FWHM increases by a factor of 1.7 - 1.3, depending on energy. Although the size increase is larger than in the case of collisional scattering, it is still not strong enough to explain the FWHM observations. In addition, a nearly isotropic initial distribution of electrons (Fig. 6) leads to a larger source FWHM at higher energies, contrary to X-ray observations.

3.5. Magnetic mirroring and collisional pitch-angle scattering

Finally, the effects described in the above two sections are combined and the full Eqs. 3-5 are solved numerically (Fig. 7). Since the effect of pitch-angle scattering itself is small compared to the effects of magnetic mirroring, this case is dominated by the effect of the magnetic field and the result very similar to the case of magnetic mirroring (Fig. 7).

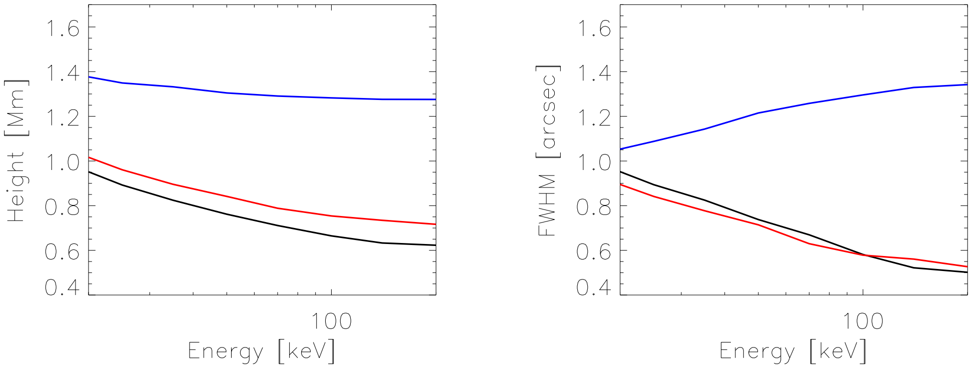

Fig. 7.— Height of maximum emission and FWHM as a function of photon energy (middle and left), for three cases of initial pitch-angle distribution: μ_0=1 (black), $0.9 < \mu_0 \leq 1$ (red), $0.1 < \mu_0 \leq 1$ (blue), and including both collisional pitch-angle scattering and magnetic mirroring.

3.6. Constructing an electron distribution as a function of height

The processes described in Sections 3.3 - 3.5 all influence the electron distribution as a function of height, e.g. pitch-angle scattering causes electrons to be stopped higher up in the loop. However, as illustrated in Fig. 5 - 7, this has a rather small effect on the X-ray flux profile and thus the source FWHM. The FWHM of an X-ray source is proportional to the product of electron flux density and plasma density $I(\epsilon, h) \sim F(E, h)n(h)$. In the extreme case of $F(E, h) \sim 1/n(h)$, the resulting $I(\epsilon, h)$ is independent of height and this constant value could extend vertically over all h where $F(E, h) \sim 1/n(h)$. We can therefore ask how $F(E, h)$ should look in order to make the product of $F(E, h)n(h)$ independent of h, hence increasing the size of the X-ray source. Starting with $F(E, h)$, as found in the simple thick target case, we modified the shape of $F(E, h)$ for every energy, so that the slope of the curve was close to $1/n(h)$, as shown in Fig. 8 (top left), then we computed the height of the maximum emission and FWHM. As $F(h)$ approaches $1/n(h)$, the FWHM of the resulting X-ray flux increases up to 5 arcsec.

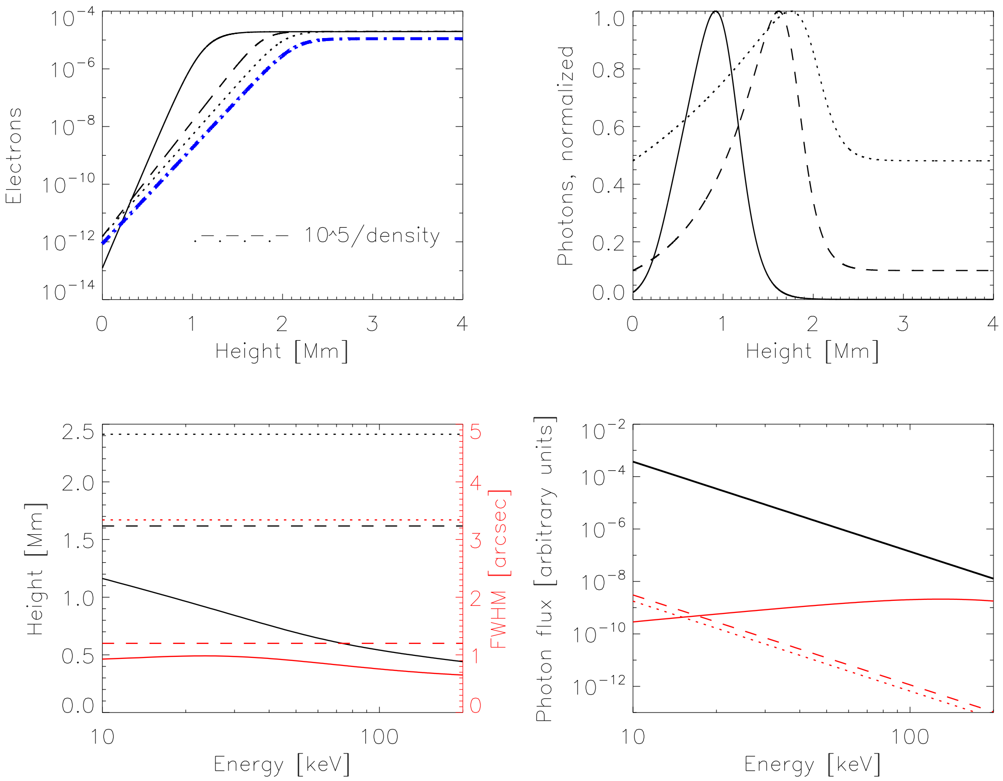

Fig. 8.— Top left: Electron flux as a function of height for 24 keV electrons. The solid line represents the simple thick target case. The dashed and dotted lines are “artificial” distributions, constructed so that the slope nears that of $1/n(h)$. The blue dash-dotted line illustrates $1/n(h)$. Top right: normalized X-ray flux. Bottom left: height and FWHM (red curves) for the three different electron distributions where the line styles correspond to the line styles in the top left panel. Bottom right: Injected electron spectrum (black line) and electron spectrum at a height of 0.8 Mm.

However, the height of the resulting HXR maximum as a function of energy is constant, as is the FWHM. Further, the electron spectrum at low heights is completely different from a thick target spectrum (Fig. 8, bottom right). Most importantly, such an electron distribution would have to be extremely “fine tuned” to the ambient density.

3.7. Instrumental effects and method

Comparing the modeling of the main electron transport effects with observations and finding physical explanations for the observed source sizes, we assumed that the observed difference is not entirely due to instrumental effects. This was based on there being no modulation in the finest RHESSI grids (Grid 1 has a spatial resolution of ~ 2.3 arcsec and grid 2 has spatial resolution ~ 3.9 arcsec) in the observed events (Battaglia & Kontar 2011), indicating that the source dimensions must be of the order of $\gtrsim 4$ arcsec. Here we perform a more quantitative study of the instrumental effects, using the simulation software developed by Richard Schwartz (private communication). The simulation software uses an arbitrary 2-dimensional map as input and creates a corresponding calibrated event list (Schwartz et al. 2002). The standard RHESSI imaging algorithms are then used to construct the image. We used several source models (circular Gaussian, elliptical Gaussian) as the initial map and forward-fitted the visibilities from the corresponding calibrated eventlist to compare the fitted FWHM with that of the original map. We find that circular Gaussians are correctly recovered within the uncertainties, e.g. a circular Gaussian with FWHM 1 arcsec is fitted with a FWHM of 0.93 ± 0.1. In the case of an elliptical Gaussian, the fitted major and minor axes tend to be larger than the original ellipse, e.g. an input elliptical source with major and minor axes of 3 and 1 arcsec respectively is fitted with 3.1 and 1.5 arcsec. Thus the fitted minor axis is 50% larger than the input minor axis.

This last example shows that, while there are instrumental effects, especially in the case of elliptical sources, these effects cannot entirely account for the observed source sizes.

The FWHM found in the previous sections are all in terms of the second moment of the 1-dimensional height distribution of X-rays $I(\epsilon, h)$. However, the limited dynamic range of RHESSI influences the accuracy of the measured moments. X-ray flux in RHESSI images which is around or less than 10% of the brightest part of the image is dominated by an error from the brightest source. However, using the simulations we can address the question of how such a source would be observed with RHESSI, and how the second moment found in the simulations relates to an observed RHESSI image. As input we used the shape of the photon-flux as a function of height found in case of a density $n(h) = n(h)^{exp} + n(h)^{\kappa}$ (green line in Fig. 2) with 6 arcsec width. This map was used as input for the simulation software and Clean and Pixon images (using software defaults and grids 1-8) were reconstructed from the calibrated event lists. Figure 9 displays the profile of the photon flux as a function of height, the input map, and the Clean and Pixon maps. The resulting fitted FWHM are $4.9''$ and $2.7''$ for the major and minor axes. The second moment of the 1-dimensional X-ray flux distribution are is $2.8''$ and becomes $2.1''$ if computed only for the emission exceeding the 10% level. Therefore, the second moment of the full distribution overestimates the size, while the moment of the flux $> 10\%$ underestimates the size, compared to visibility forward fitting. It has to be added that the source model was very simple and there is no unmodulated background added to calibrated event lists.

4. Summary and conclusions

In the simple collisional thick-target model, both the height of the maximum HXR emission and the vertical HXR source sizes are determined by the density scale height. RHESSI observations suggest that the HXR source positions can be well fitted with a single exponential scale-height density model, assuming a simple collisional thick target. This results in scale heights between about 130 km and 200 km (Kontar et al. 2008, 2010; Battaglia & Kontar 2011), consistent with chromospheric models (e.g. Machado et al. 1980; Vernazza et al. 1981). However, the observed HXR sizes are about 4 times larger than expected from the simple collisional transport model. Here we have quantitatively investigated how the density profile, collisional pitch-angle scattering, magnetic mirroring, as well as instrumental effects affect the source sizes.

In Battaglia & Kontar (2011) we showed that projection effects and source motion over the RHESSI image time interval cannot account for the observed source sizes. In the present work, applying RHESSI visibility forward fitting on simulated HXR source maps we demonstrate that the source size cannot be due to instrumental effects, alone. This leaves the physical effects of magnetic mirroring and collisional pitch-angle scattering which we investigate by solving the Fokker-Planck equation both numerically and analytically. While pitch angle and magnetic mirroring effects change the electron flux distribution, these effects tend to increase the FWHM of the X-ray source profile by only up to a factor 1.5, which is not enough to explain the observations. The dominating factor that determines the X-ray source size is the atmospheric density structure. In the case of an exponential density model with a single scale height and a constant coronal loop density of around 10^{10} cm^{-3}, the X-ray emission will originate predominantly from the region of highest density. Thus, even though the effects described above alter the electron distribution as a function of height, emission by electrons higher up in the loop will always be faint compared to the emission from the

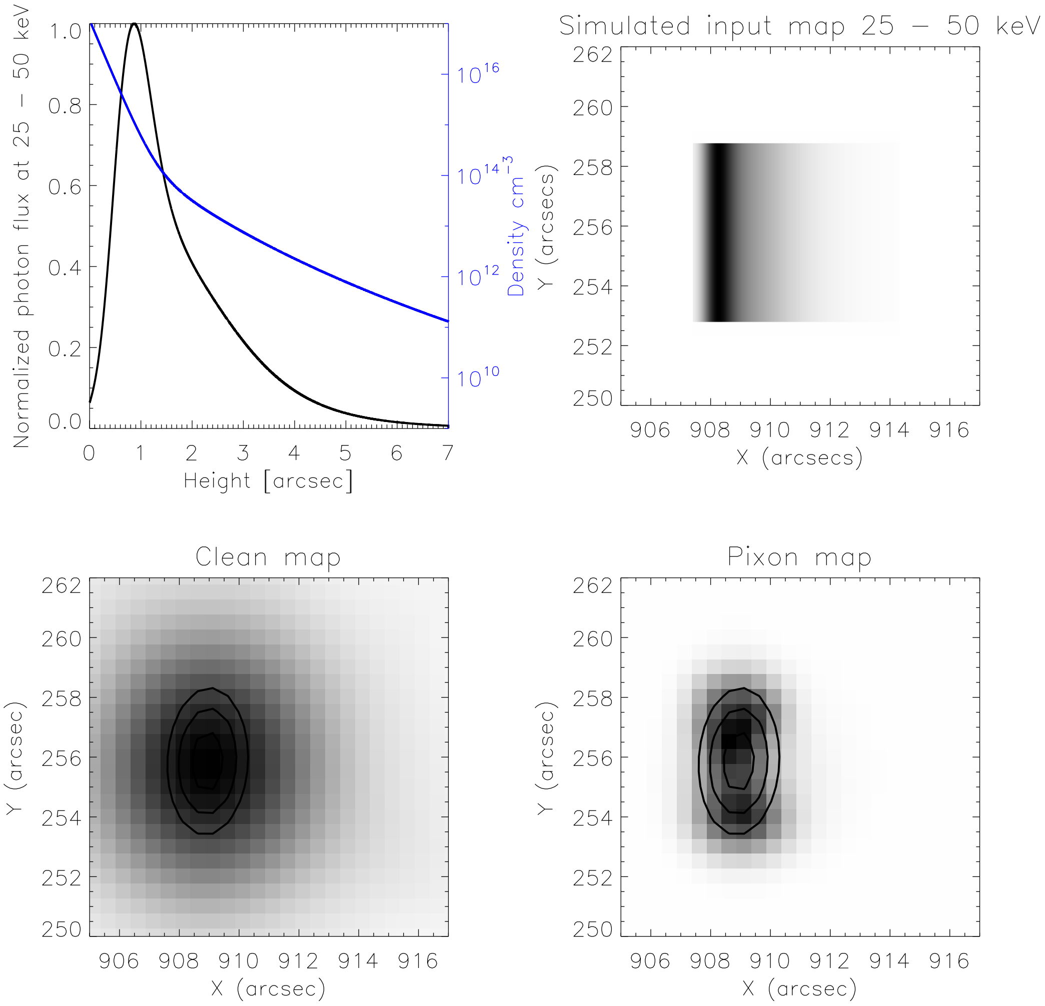

Fig. 9.— Top left: X-ray (black) profile for simulations with high loop density (blue). Top right: Simulated map of a loop with ∼ 6 arcsec width and the height profile of the simulated X-ray profile. Bottom: RHESSI CLEAN and Pixon image representation of the simulated map. The contours represent the 50%, 70%, and 90% levels of the elliptical Gaussian found with visibility forward fitting.

denser chromosphere. Source sizes of around 4 arcseconds can only be achieved by unlikely loop densities of the order of 10^{13} cm^{-3}. Such high densities will also cause the HXR sources to appear at larger heights, well above typical chromospheric heights. Thus, within the traditional thick target model, the only plausible explanation for the observed HXR source sizes remains a multi-threaded density structure.

This work is supported by the Leverhulme Trust (M.B., E.P.K., L.F.) and STFC grant ST/I001808 (E.P.K., L.F., A.L.M). Financial support by the European Commission through the FP7 HESPE network (FP7-2010-SPACE-263086) is gratefully acknowledged. We thank Richard Schwartz for providing and helping with the RHESSI image simulation software and Gordon Hurford for discussions.

REFERENCES

Allred, J. C., Hawley, S. L., Abbett, W. P., & Carlsson, M. 2005, ApJ, 630, 573

Antiochos, S. K., & Sturrock, P. A. 1978, ApJ, 220, 1137

Aschwanden, M. J., Brown, J. C., & Kontar, E. P. 2002, Sol. Phys., 210, 383

Bai, T. 1982, ApJ, 259, 341

Battaglia, M., & Kontar, E. P. 2011, ApJ, 735, 42

Brown, J. C. 1973, Sol. Phys., 28, 151

Fedun, V., Verth, G., Jess, D. B., & Erdélyi, R. 2011, ApJ, 740, L46

Fletcher, L. 1996, A&A, 310, 661

Hirayama, T. 1974, Sol. Phys., 34, 323

Holman, G. D., Aschwanden, M. J., Aurass, H., et al. 2011, Space Sci. Rev., 159, 107

Hurford, G. J., Schmahl, E. J., Schwartz, R. A., et al. 2002, Sol. Phys., 210, 61

Kocharov, L., Kovaltsov, G. A., & Torsti, J. 2000, ApJ, 543, 438

Kontar, E. P., Brown, J. C., & McArthur, G. K. 2002, Sol. Phys., 210, 419

Kontar, E. P., Hannah, I. G., Jeffrey, N. L. S., & Battaglia, M. 2010, ApJ, 717, 250

Kontar, E. P., Hannah, I. G., & MacKinnon, A. L. 2008, A&A, 489, L57

Kovalev, V. A., & Korolev, O. S. 1981, Soviet Ast., 25, 215

Leach, J., & Petrosian, V. 1981, ApJ, 251, 781

—. 1983, ApJ, 269, 715

Lin, R. P., Dennis, B. R., Hurford, G. J., et al. 2002, Sol. Phys., 210, 3

Machado, M. E., Avrett, E. H., Vernazza, J. E., & Noyes, R. W. 1980, ApJ, 242, 336

MacKinnon, A. L., & Craig, I. J. D. 1991, A&A, 251, 693

McClements, K. G. 1990, A&A, 234, 487

—. 1992, A&A, 253, 261

Minoshima, T., Yokoyama, T., & Mitani, N. 2008, ApJ, 673, 598

Petrosian, V., & Donaghy, T. Q. 1999, ApJ, 527, 945

Saint-Hilaire, P., Krucker, S., & Lin, R. P. 2010, ApJ, 721, 1933

Schmahl, E. J., Pernak, R. L., Hurford, G. J., Lee, J., & Bong, S. 2007, Sol. Phys., 240, 241

Schwartz, R. A., Csillaghy, A., Tolbert, A. K., et al. 2002, Sol. Phys., 210, 165

Vernazza, J. E., Avrett, E. H., & Loeser, R. 1981, ApJS, 45, 635

Veronig, A. M., Karlický, M., Vršnak, B., et al. 2006, A&A, 446, 675

Zweibel, E. G., & Haber, D. A. 1983, ApJ, 264, 648

This preprint was prepared with the AAS LaTeX macros v5.2.